Single YVO_4:Eu nanoparticle emission spectra using direct Eu^{3+} ion excitation with a sum-frequency 465-nm solid-state laser

Thanh-Liêm Nguyên,[1] Marc Castaing,[2] Thierry Gacoin,[3] Jean-Pierre Boilot,[3] François Balembois,[2] Patrick Georges,[2] and Antigoni Alexandrou[1,*]

[1]*Laboratoire d'Optique et Biosciences, Ecole Polytechnique, CNRS, INSERM U696, 91128 Palaiseau, France*
[2]*Laboratoire Charles Fabry, UMR 8501, Institut d'Optique, CNRS, Univ. Paris Sud 11, 2 avenue Augustin Fresnel, 91127 Palaiseau Cedex, France*
[3]*Laboratoire de Physique de la Matière Condensée, Ecole Polytechnique, CNRS, 91128 Palaiseau, France*
[*]*antigoni.alexandrou@polytechnique.edu*

Abstract: We report emission spectrum measurements on single $Y_xEu_{1-x}VO_4$ nanoparticles. The inhomogeneous widths of the emission peaks are identical for single nanoparticles and for ensembles of nanoparticles, while being broader than those of the bulk material. This indicates that individual nanoparticles are identical in terms of the distribution of different local Eu^{3+} sites due to crystalline defects and confirms their usability as identical, single-particle oxidant biosensors. Moreover, we report a 465 nm solid-state laser based on sum-frequency mixing that provides a compact, efficient solution for direct Eu^{3+} excitation of these nanoparticles. Both these two aspects should broaden the scope of Eu-doped nanoparticle applications.

References and links

1. C. Bouzigues, T. Gacoin, and A. Alexandrou, "Biological applications of rare-earth based nanoparticles," ACS Nano **5**(11), 8488–8505 (2011).
2. K. Riwotzki and M. Haase, "Wet-chemical synthesis of doped colloidal nanoparticles: YVO_4:Ln (Ln = Eu, Sm, Dy)," J. Phys. Chem. B **102**(50), 10129–10135 (1998).
3. A. Huignard, T. Gacoin, and J.-P. Boilot, "Synthesis and luminescence properties of colloidal YVO_4:Eu phosphors," Chem. Mater. **12**(4), 1090–1094 (2000).
4. A. Son, A. Dhirapong, D. K. Dosev, I. M. Kennedy, R. H. Weiss, and K. R. Hristova, "Rapid and quantitative DNA analysis of genetic mutations for polycystic kidney disease (PKD) using magnetic/luminescent nanoparticles," Anal. Bioanal. Chem. **390**(7), 1829–1835 (2008).
5. D. Dosev, M. Nichkova, M. Liu, B. Guo, G. Y. Liu, B. D. Hammock, and I. M. Kennedy, "Application of luminescent Eu:Gd_2O_3 nanoparticles to the visualization of protein micropatterns," J. Biomed. Opt. **10**(6), 064006 (2005).
6. E. Beaurepaire, V. Buissette, M.-P. Sauviat, D. Giaume, K. Lahlil, A. Mercuri, D. Casanova, A. Huignard, J.-L. Martin, T. Gacoin, J.-P. Boilot, and A. Alexandrou, "Functionalized fluorescent oxide nanoparticles: artificial toxins for sodium channel targeting and imaging at the single-molecule level," Nano Lett. **4**(11), 2079–2083 (2004).
7. J.-B. Masson, D. Casanova, S. Türkcan, G. Voisinne, M. R. Popoff, M. Vergassola, and A. Alexandrou, "Inferring maps of forces inside cell membrane microdomains," Phys. Rev. Lett. **102**(4), 048103 (2009).
8. S. Türkcan, J.-B. Masson, D. Casanova, G. Mialon, T. Gacoin, J.-P. Boilot, M. R. Popoff, and A. Alexandrou, "Observing the confinement potential of bacterial pore-forming toxin receptors inside rafts with nonblinking Eu^{3+}-doped oxide nanoparticles," Biophys. J. **102**(10), 2299–2308 (2012).
9. S. Türkcan, M. U. Richly, A. Alexandrou, and J.-B. Masson, "Probing membrane protein interactions with their lipid raft environment using single-molecule tracking and Bayesian inference analysis," PLoS ONE **8**(1), e53073 (2013).
10. S. Türkcan, M. U. Richly, C. I. Bouzigues, J.-M. Allain, and A. Alexandrou, "Receptor displacement in the cell membrane by hydrodynamic force amplification through nanoparticles," Biophys. J. **105**(1), 116–126 (2013).

11. D. Casanova, C. Bouzigues, T.-L. Nguyên, R. O. Ramodiharilafy, L. Bouzhir-Sima, T. Gacoin, J.-P. Boilot, P.-L. Tharaux, and A. Alexandrou, "Single europium-doped nanoparticles measure temporal pattern of reactive oxygen species production inside cells," Nat. Nanotechnol. **4**(9), 581–585 (2009).
12. C. I. Bouzigues, T.-L. Nguyên, R. O. Ramodiharilafy, A. Claeson, P.-L. Tharaux, and A. Alexandrou, "Regulation of the ROS response dynamics and organization to PDGF motile stimuli revealed by single nanoparticle imaging," Chem. Biol. **21**(5), 647–656 (2014).
13. M. Schoeffel, M. Abdesselem, I. Maurin, G. Autret, O. Clément, J.-P. Boilot, T. Gacoin, C.I. Bouzigues, and A. Alexandrou, Submitted.
14. D. Casanova, D. Giaume, E. Beaurepaire, T. Gacoin, J.-P. Boilot, and A. Alexandrou, "Optical in situ size determination of single lanthanide-ion doped oxide nanoparticles," Appl. Phys. Lett. **89**(25), 253103 (2006).
15. K. Riwotzki and M. Haase, "Colloidal YVO_4:Eu and $YP_{0.95}V_{0.05}O_4$:Eu nanoparticles: luminescence and energy transfer processes," J. Phys. Chem. B **105**(51), 12709–12713 (2001).
16. A. Huignard, V. Buissette, A.-C. Franville, T. Gacoin, and J.-P. Boilot, "Emission processes in YVO_4:Eu nanoparticles," J. Phys. Chem. B **107**(28), 6754–6759 (2003).
17. G. Mialon, M. Gohin, T. Gacoin, and J.-P. Boilot, "High temperature strategy for oxide nanoparticle synthesis," ACS Nano **2**(12), 2505–2512 (2008).
18. G. Mialon, S. Türkcan, A. Alexandrou, T. Gacoin, and J.-P. Boilot, "New insights into size effects in luminescent oxide nanocrystals," J. Phys. Chem. C **113**(43), 18699–18706 (2009).
19. To our knowledge, only the company Modulight proposes custom-made diode lasers at 465 nm, www.modulight.com.
20. D. Woll, B. Beier, K. J. Boller, R. Wallenstein, M. Hagberg, and S. O'Brien, "1 W of blue 465-nm radiation generated by frequency doubling of the output of a high-power diode laser in critically phase-matched LiB_3O_5.," Opt. Lett. **24**(10), 691–693 (1999).
21. K. Li, H. Wang, N. J. Copner, C. B. E. Gawith, I. G. Knight, H.-U. Pfeiffer, B. Musk, and G. Moss, "465 nm laser sources by intracavity frequency doubling using a 49-edge-emitters laser bar," Opt. Lett. **36**(3), 361–363 (2011).
22. Y. L. Li, H. L. Jiang, W. Liang, T. Y. Ni, T. Y. Zhang, Z. H. Tao, and Y. H. Zeng, "Quasi-three level laser based on diode-pumped Nd^{3+}:$YAlO_3$ crystal," Laser Phys. **21**(5), 897–900 (2011).
23. T. Baer, "Large-amplitude fluctuations due to longitudinal mode-coupling in diode-pumped intracavity-doubled Nd-YAG lasers," J. Opt. Soc. Am. B **3**(9), 1175–1180 (1986).
24. P. J. Cutler, M. D. Malik, S. Liu, J. M. Byars, D. S. Lidke, and K. A. Lidke, "Multi-color quantum dot tracking using a high-speed hyperspectral line-scanning microscope," PLoS ONE **8**(5), e64320 (2013).
25. C. Brecher, H. Samelson, A. Lempicki, R. Riley, and T. Peters, "Polarized spectra and crystal-field parameters of Eu^{+3} in YVO_4," Phys. Rev. **155**(2), 178–187 (1967).
26. B. R. Judd, "Optical absorption intensities of rare-earth ions," Phys. Rev. **127**(3), 750–761 (1962).
27. G. S. Ofelt, "Intensities of crystal spectra of rare-earth ions," J. Chem. Phys. **37**(3), 511 (1962).
28. O. Lehmann, K. Kömpe, and M. Haase, "Synthesis of Eu3+-doped core and core/shell nanoparticles and direct spectroscopic identification of dopant sites at the surface and in the interior of the particles," J. Am. Chem. Soc. **126**(45), 14935–14942 (2004).
29. B. Fleury, M. A. Neouze, J. M. Guigner, N. Menguy, O. Spalla, T. Gacoin, and D. Carriere, "Amorphous to crystal conversion as a mechanism governing the structure of luminescent YVO4:Eu nanoparticles," ACS Nano **8**(3), 2602–2608 (2014).

1. Introduction

Biological and biomedical applications generate a strong demand for nanoparticle-based luminescent labels, sensors, imaging contrast agents or for nanoparticles as platforms for targeting and therapy approaches. In all these cases, the luminescent properties are crucial. Indeed, even when optical imaging is not the main application, it is highly desirable to be able to locate the nanoparticles in cells or in tissues.

Besides semiconductor quantum dots (QDs) and luminescent nanodiamonds, rare-earth based nanoparticles concentrate the efforts of numerous groups [1]. Eu-doped nanoparticles, in particular, are quite popular because of the efficient, red emission of Eu^{3+} ions [2,3]. In addition to DNA [4] and protein assay applications [5], we have shown that Eu-doped oxide nanoparticles are excellent single-molecule labels [6]. Indeed, they present stable, narrow-band (<10 nm) emission resulting from 4f-4f transitions, display no blinking, in contrast to quantum dots, and can therefore be used for long-term, uninterrupted single-molecule tracking [7–10]. Furthermore, we have demonstrated that oxido-reduction processes of Eu ions in an yttrium vanadate matrix can be exploited to create a quantitative, time- and space-resolved oxidant sensor [11,12]. More recently, we have also implemented multifunctional Eu-doped nanoparticles by replacing yttrium with gadolinium which provide simultaneously

luminescence labeling, oxidant sensing and contrast enhancement in magnetic resonance imaging (MRI) [13].

The in-depth structural and optical characterization of such nanoparticles is important for all these applications. In single-molecule tracking and oxidant sensing applications, where single nanoparticles are used, it is crucial to determine whether the signal may differ depending on the particular nanoparticle observed or not, i.e. whether the optical emission properties vary from one particle to the other. In the case of sensing and MRI imaging applications, the access of the oxidant and the water molecules, respectively, into the nanoparticle structure depends on its porosity. In that respect, we demonstrated that oxidant sensing signal variations from one nanoparticle to the other are small for different single nanoparticles [11,12]. Furthermore, we have shown that the emission intensity of single nanoparticles can be used to optically determine their size [14]. This method implicitly assumes that all nanoparticles are identical in terms of optical emission properties.

The emission properties of colloidal solutions of YVO_4:Eu nanoparticles have been addressed in [2,3,15,16]. Mialon et al. investigated the emission properties of an ensemble of YVO_4:Eu nanoparticles in comparison to those of annealed nanoparticles [17] and the bulk material and demonstrated that the emission was limited by defects affecting energy transfer and non radiative relaxation as well as by dielectric effects affecting radiative lifetime and thus quantum yield [18]. This means that the structural properties at the single-particle level, such as crystallinity and porosity, are determinant for the emission and sensor properties of these particles, in particular for nanoparticles synthesized at room temperature in which lattice imperfections are more abundant [17].

In rare-earth doped nanoparticles, the highly localized, atomic-like nature of the f electronic states ensures weak interaction with the surrounding lattice and narrow emission peaks. However, the presence of a large number of dopant ions and of multiple local dopant ion environments leads to transition energy variations and subsequently to an increase of the emission spectral width reflecting the nanoparticle internal structural heterogeneity. Inhomogeneous broadening is thus predominant even at room temperature [18]. This means that, in the case of rare-earth doped nanoparticles, structural information on single particles can be obtained from their spectra. In contrast, in the case of QDs at room temperature, the lifetime of the electronic states is dominated by the electron-phonon interaction, the resulting emission width (~25 nm) is homogeneous, and structural information can only be obtained by performing spectral measurements at low temperatures.

An issue that may limit the range of *in vivo* applications of Eu-based nanoparticles, is their excitation possibilities. For *in vitro* applications, excitation of the matrix in the UV and subsequent energy transfer to Eu ions may be used even though excitation sources are scarce. For *in vivo* applications, however, direct excitation of Eu ions in the visible is preferable to avoid UV laser-induced phototoxicity [6–8]. In our previous work, the 465.8-nm Argon-ion laser line has been used to excite Eu^{3+} ions in resonance with the $^7F_{0,1} - ^5D_2$ Eu^{3+} transition. For a more widespread use of these nanoparticles, however, the availability of a compact, inexpensive, and easily transportable excitation source at the appropriate wavelength is important.

We here present a solid-state, compact 465-nm laser that may conveniently replace the Argon-ion laser used up to now to excite Eu-doped nanoparticles. Using this laser, we realized, to our knowledge, the first measurement of single Eu-doped nanoparticle emission spectra. Based on these data, we may conclude that, although crystalline imperfections in the nanoparticles induce a broadening of the emission peaks, the inhomogeneity of the Eu^{3+}-ion local environments is similar in all individual nanoparticles, *i.e.* the nanoparticles are identical in terms of structural inhomogeneity.

2. 465-nm solid-state laser

Today, GaN laser diodes cover a wide range of wavelengths in the blue but not continuously. It appears that 465 nm corresponds precisely to a hole of emission. Laser diodes at this emission wavelength are difficult to obtain [19]. Fortunately, this wavelength can be obtained by frequency conversion of near-infrared laser sources. In the past, frequency doubling has been carried out: direct frequency conversion of laser diodes has been developed in an external resonant cavity with an LBO crystal [20] or in an intracavity configuration with periodically poled lithium niobate [21] leading to output power of up to 1 W. Diode-pumped Nd:YAP ($YAlO_3$) laser emitting at 930 nm and frequency doubled by an LBO crystal in an intracavity configuration has produced up to 1.13 W [22]. In this work, we tried another nonlinear conversion scheme to reach 465 nm, based on the sum frequency mixing of two Nd emission wavelengths (914 nm and 946 nm) in two different host matrices (YAG and YVO_4). This solution presents the advantage of being less sensitive to intrinsic fluctuations due to longitudinal mode coupling in intracavity frequency-doubled lasers [23]. Moreover, this scheme is more simple than external frequency doubling which required active control of the resonant cavity on the laser cavity [20].

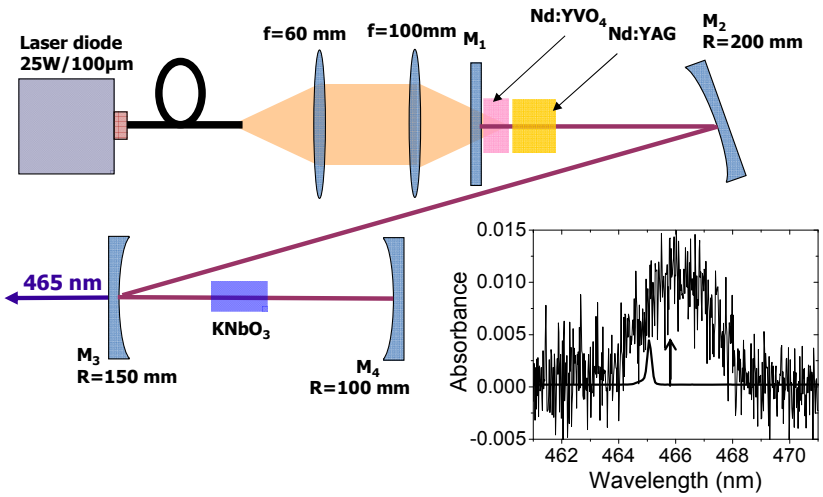

Fig. 1. Layout of the solid-state sum-frequency 465-nm laser. The inset shows the absorbance of a dense colloidal $Y_{0.6}Eu_{0.4}VO_4$ nanoparticle solution in the spectral range of the $^7F_{0,1} - ^5D_2$ Eu^{3+} transition (the background slope due to diffusion has been subtracted) together with the emission spectrum of the sum-frequency 465-nm solid-state laser. The arrow shows the Argon-ion emission line.

Our laser source is based on the sum-frequency mixing of two lasers operating in the same cavity: a Nd:YAG laser operating at 946 nm and a Nd:YVO_4 laser operating at 914 nm (Fig. 1). The crystals are pumped by the same fiber-coupled laser diode emitting 14.4 W from a 100-µm core fiber having a numerical aperture of 0.2. The pump beam is collimated and focused down to 170 µm diameter in the laser crystals by two doublets having focal lengths of 60 mm and 100 mm, respectively. As laser emission at 914 nm needs a more important population inversion than laser emission at 946 nm, the first crystal to be pumped is Nd:YVO_4 (length: 1.5 mm; doping concentration: 0.1%). The Nd:YAG (length: 3.5 mm; doping concentration: 0.5%) crystal is placed very close to the vanadate crystal in the same copper mount. The overall absorption by the two crystals is 63%. The laser cavity consists of four mirrors having two small waists: one for the laser crystals, adapted to the pump (radius 80 µm) and one for the nonlinear crystal (radius 50 µm). The latter is a potassium niobate crystal ($KNbO_3$) cut for sum frequency conversion (37° with respect to the ba plane) with a length of 4 mm. Because of the small thermal acceptance of this nonlinear crystal, its temperature was

stabilized at 25°C with an accuracy better than 0.1°C. The four mirrors of the cavity were highly reflective in the range 900-950 nm. The input mirror (M1) was transparent at 808 nm and M4 was also highly reflective at 465 nm in order to have only one output in the blue, through M3. In addition, M2, M3, and M4 were highly transparent around 1070 nm to avoid laser oscillation at the strong four-level laser line at 1064 nm for Nd:YVO_4 and 1080 nm for Nd:YAP. At 14.4 W of incident pump power, we achieved an output power of 100 mW at 465.1 nm which is high enough for all applications using YVO_4:Eu nanoparticles including single-molecule tracking and oxidant detection.

3. Experimental

The nanoparticles are synthesized by salt coprecipitation at room temperature following [3]. An aqueous solution of 0.1 M Na_3VO_4 is freshly prepared and its pH is adjusted between 12.6 and 13 with a 1 M NaOH solution. The same volume of a 0.1-M aqueous solution of $(Y,Eu)(NO_3)_3$ with the desired europium content (here the molar fraction was 10% or 40%) is then added dropwise using a peristaltic pump under vigorous stirring. The solution is left under stirring for 30 min and is then purified by centrifugations (11400g, 20 min) and redispersions in pure water until its conductivity is below 100 $\mu S.cm^{-1}$. Before imaging the nanoparticles, we performed size selection using centrifugation: 5 min at 2000 g (the supernatant was retained) followed by 30 min at 4000 g (the precipitate was retained and re-dispersed) to eliminate aggregates or large nanoparticles and small nanoparticles, respectively. This leads to a nanoparticle size distribution of 20-70 nm. Note that these particles contain tens of thousands of Eu^{3+} ions: given the fact that the volume of the unit cell is 0.323 nm^3 and contains four vanadate and four Y^{3+}/Eu^{3+} ions, a 30-nm particle $Y_{0.6}Eu_{0.4}VO_4$ contains about 70 000 Eu^{3+} ions [14]. Moreover, the Eu^{3+} ions have been shown to be homogeneously incorporated in Y^{3+} sites based on the fact that the lattice parameter of $Y_{1-x}Eu_xVO_4$ nanoparticles as a function of Eu concentration follows Veggard's rule [3]. To synthesize the bulk material, the nanoparticle solution was dried in an oven and annealed at 1000 °C for 10 h [18].

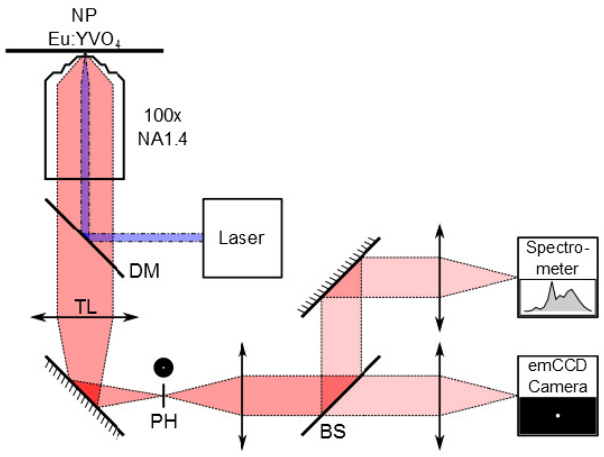

Fig. 2. Scheme of the experimental set-up. DM: dichroic mirror, TL: Tube lens, PH: diaphragm, BS: beam-splitter.

$Y_xEu_{1-x}VO_4$ nanoparticles (x = 0.1 or x = 0.4) were spincoated on glass coverslips and were imaged with a wide-field microscope (Zeiss AxioObserver D1) equipped with a 63x, N.A. = 1.4 plan-apochromat objective. The nanoparticles were excited with 25 mW focused down to a FWHM of 95 µm at the coverslip. The emitted light was collected though a

dichroic mirror (500DRLP, Omega). After the tube lens, an afocal lens system with a beamsplitter splits the emission in two (Fig. 2). The first part is used to spatially image the nanoparticles with a CCD camera (Roper Scientific LN/CCD-400-PB, 400x1340 20-µm pixels), whereas the second is sent into a spectrometer (Jobin Yvon HR25, slit width: 200 µm, spectral resolution: 0.3 nm) and detected with a second CCD camera (Roper Scientific 7488-0001) to measure the spectrum. For spectral measurements on nanoparticle ensembles, we deposit a drop of nanoparticle solution on the coverslip. For spectral measurements on single nanoparticles, we dilute the nanoparticle solution used for the spincoating so that only a few nanoparticles are visible in the spatial image registered with the first camera. A diaphragm is then inserted in the intermediate focal place before the afocal lens system to isolate a single nanoparticle.

The spatial image [Fig. 3(A)] ensures that we are indeed detecting the spectrum of a single particle [Fig. 3(B)]. First, the emission spot is diffraction limited: it typically is 2-3 pixels wide corresponding to a FWHM of 400 nm. Second, for each nanoparticle analyzed, we determined the total number of collected photons and from that calculated its size, as demonstrated in [14]. In our case, the quantum yield of the nanoparticles was 13% and the collection efficiency of the optical setup was 5%. For the 15 10% Eu-doped nanoparticles analyzed, we found total detected photon numbers ranging from 230 to 1867 photons yielding sizes ranging from 36 nm to 72 nm with a mean value and standard deviation of 53.1 (± 11.4) nm. For the 14 40% Eu-doped nanoparticles, we found total detected photon numbers ranging from 199 to 6145 photons yielding sizes ranging from 22 nm to 68 nm with a mean value and standard deviation of 42.9 (± 14.3) nm. Note that the photon numbers emitted by the 40% Eu-doped particles are higher than those emitted by 10% Eu-doped particles for the same excitation intensity and particle size because the particle absorption is proportional to the number of Eu ions in the particle.

Long acquisition times (a few minutes) are required to obtain the emission spectra of single particles with a signal-to-noise ratio sufficient for analysis of the different spectral contributions. Indeed, for particles of about 30 nm, a few hundred photons are typically collected in 50 ms [8]. Spreading these photons over 1340 pixels to realize the spectral measurements means that long averaging is necessary to collect photon numbers per pixel with sufficient signal-to-noise ratio. Note that the high-speed hyperspectral microscope reported in [24] for multi-color QD tracking based on the distinct spectral characteristics of individual QDs relies on spectral filtering of single QD emission but does not measure the full spectrum of each QD.

4. Results and discussion

We first verified the excitation efficiency of $Y_{0.6}Eu_{0.4}VO_4$ nanoparticles by our solid-state laser. After spincoating the nanoparticles on a glass coverslip, we excited the same coverslip area using alternatively the sum-frequency laser and the Argon-ion 465.8 nm laser line at the same excitation intensity and determined the total number of detected photons per emission spot with each laser. The average ratio of emitted signal excited by the solid-state and the Argon laser at a power of 50 mW focused down to approximately 20 µm was 0.76 (N = 19 nanoparticles). This is in agreement with the fact that the sum-frequency laser wavelength does not correspond precisely to the maximum of the $^7F_{0,1} - ^5D_2$ Eu^{3+} direct absorption peak in the YVO_4 matrix (see inset of Fig. 1).

The Eu^{3+} site in bulk YVO_4 has no inversion symmetry. In this case, the selection rule for electrical dipole transitions is $|\Delta J| = 2,4,6$ if the initial or final state has $J = 0$ and $|\Delta J| \leq 6$ otherwise. We here focus on the wavelength range of the most intense Eu^{3+} $^5D_0 - ^7F_2$ emission (600-620 nm). Depending on the symmetry of the host lattice and of the Eu^{3+} site, the Eu^{3+} energy levels can be split into up to 2J + 1 sublevels, i. e. one sublevel for $^5D_0$ and five sublevels for $^7F_2$. The Eu^{3+} site in YVO_4 single crystals has D_{2d} symmetry. This crystal field

symmetry leads to a splitting of the fivefold $^5D_0$–$^7F_2$ transitions into two: $^5D_0(A_1)$–$^7F_2(B_2)$ and $^5D_0(A_1)$–$^7F_2(E)$ [25].

The spectrum of single YVO_4:Eu nanoparticles displays five peaks that can be fitted with five Lorentzians with center wavelengths 608.74 nm, 613.85 nm, 614.84 nm, 616.65 nm, 618.70 nm [Fig. 3(B)]. These emission peaks can be attributed to the transitions $^5D_0(A_1)$–$^7F_2(B_2)$ and $^5D_0(A_1)$–$^7F_2(E)$ observed in bulk YVO_4:Eu at 615.5 nm and 619.4 nm, respectively [2,3,15,16,25]. Note that, at low temperature, transitions starting from the $^5D_2$ level and the $^5D_1$ level have also been reported for bulk YVO_4:Eu in this wavelength range, in particular $^5D_2(A_1)$–$^7F_6(B_2^{(1)})$ at 609.7 nm, $^5D_2(E)$–$^7F_6(A_2)$ at 611.7 nm, $^5D_2(E)$–$^7F_6(E^{(1)})$ at 613.3 nm, and $^5D_1(A_2)$–$^7F_4(B_1)$ at 616.1 nm [25]. At room temperature, however, transitions departing from the $^5D_1$ and $^5D_2$ levels are at least 100 times weaker than those departing from the $^5D_0$ level [15] due to more efficient de-excitation to the lowest lying ^5D energy level, $^5D_0$, before radiative de-excitation takes place. The presence of five peaks instead of two may possibly be attributed to crystalline imperfections leading to a reduced symmetry of the Eu^{3+} sites with respect to the bulk crystal and thus causing further degeneracy lifting.

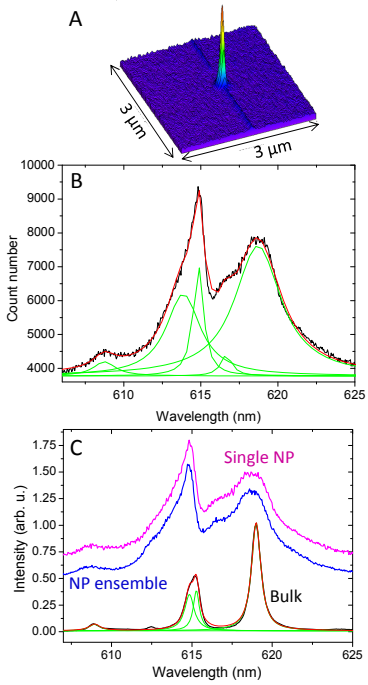

Fig. 3. A) Spatial image of the sample area whose emission is recorded with the spectrometer and the CCD detector. A single diffraction-limited nanoparticle emission spot is observed. B) Emission spectrum of the $Y_{0.6}Eu_{0.4}VO_4$ nanoparticle in A) (black; excitation power: 25 mW; acquisition time: 300 s) together with the five Lorentzian peaks used to fit the spectrum (green) and the resulting fit (red). C) Comparison between the single-nanoparticle emission spectrum in B) (magenta), the emission spectrum of an ensemble of $Y_{0.6}Eu_{0.4}VO_4$ nanoparticles (blue; excitation power: 25 mW; acquisition time: 300 ms), and the emission spectrum of bulk $Y_{0.5}Eu_{0.5}VO_4$ (black) together with the four Lorentzian peaks used to fit the spectrum (green) and the resulting fit (red). The single nanoparticle and the nanoparticle ensemble spectra have been displaced vertically for clarity.

Local deviations from the D_{2d} symmetry also lead to intensity and width variations [26,27]. Indeed, the widths of the nanoparticle emission peaks are much broader that those of bulk samples [Fig. 3(C)]. This has been reported previously for nanoparticle ensembles together with the observation that annealed, monocrystalline nanoparticles [17] display much narrower widths, close to those of bulk material [18]. The larger width is due to the lower

crystalline quality of the nanoparticles and can be interpreted as follows: in a nanoparticle, crystalline imperfections create a local environment that is somewhat different for different Eu^{3+} ions in the same nanoparticle leading to slightly varying Eu^{3+}-ion transition energies. This collection of distinct environments and the resulting transition energies lead to a broadening of the emission peaks. Note also that, when fitting the spectra with a series of Lorentzian peaks, the bulk material spectrum shows no trace of the 616.65 nm transition peak, in agreement with the presence of a higher symmetry in the bulk material [Fig. 3(C)].

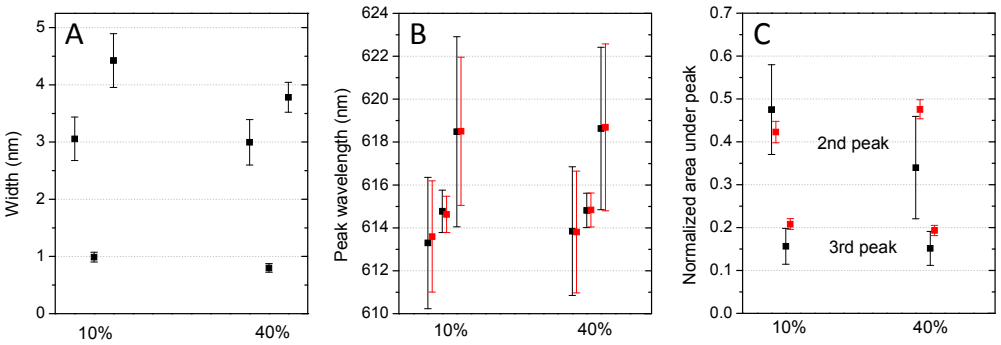

Fig. 4. A) Widths of the first, third and fifth Lorentzian peaks at 608.74, 614.84, and 618.70 nm (shown from left to right) used to reproduce the emission spectra of single $Y_xEu_{1-x}VO_4$ nanoparticles for x = 0.1 and 0.4. The error bars represent the standard deviation of the measurements for 15 and 14 single nanoparticles with 10% and 40% europium, respectively. B) Center wavelength of the first, third and fifth Lorentzian peaks used to reproduce the emission spectra of single $Y_xEu_{1-x}VO_4$ nanoparticles (black) and of an ensemble of $Y_xEu_{1-x}VO_4$ nanoparticles (red) for x = 0.1 and 0.4. The error bars represent the FWHM of the corresponding peaks. For single nanoparticles, the average FWHM is shown [see A)]. C) Emission peak area of the second and third Lorentzians used to reproduce the emission spectra for single $Y_xEu_{1-x}VO_4$ nanoparticles (black) and for an ensemble of particles (red) for x = 0.1 and 0.4 normalized to the peak area of the fifth Lorentzian. The error bars represent the standard deviation of the measurements for 15 and 14 single nanoparticles with 10% and 40% europium, respectively.

In contrast, the spectrum of single nanoparticles is practically identical to that of a collection of particles [Fig. 3(C)]. The question that arises is whether all nanoparticles are "identical", i. e. whether they all feature the same collection of local environments for Eu^{3+} ions. To further address this question, we measured the spectra of 15 (14) single $Y_xEu_{1-x}VO_4$ nanoparticles for x = 0.1 (0.4) and fitted the spectra with five Lorentzian peaks as in Fig. 3B. We then plotted the FWHM of the different peaks, indicative of the crystalline imperfections, and, in particular, its average value and standard deviation [Fig. 4(A)]. The small standard deviation indicates the similarity of local environment distributions inside different individual nanoparticles. Moreover, the center wavelengths and the corresponding widths of the three main Lorentzian peaks used to reproduce single nanoparticle spectra [Fig. 4(B)] as well as the emission peak areas [Fig. 4(C)] agree surprisingly well with those of nanoparticle ensemble spectra.

These data lead us to conclude that each single nanoparticle encompasses the same distribution of locally different Eu^{3+}-ion environments including Eu^{3+} ions at the surface and at the core of the nanoparticles [28]. Therefore, each nanoparticle features the same deviation from a perfect crystalline environment. This similarity of the ensemble of lattice defects found in different nanoparticles is a non trivial result. Moreover, it may seem surprising given the size dispersion of the nanoparticles. Indeed, the weight of surface ions may be expected to be more important in smaller nanoparticles than in bigger ones. However, current knowledge on

the growth process of these nanoparticles provides an explanation to our observations. Nanoparticle growth is considered to proceed by aggregation of primary grains [29]. This means that the ratio of surface to core ions remains the same independently of the size of the nanoparticles. Our observation that all nanoparticles contain the same collection of local Eu^{3+}-ion environments thus implies that these primary grains are identical in terms of crystallinity.

Our results justify the assumption that the total area under the emission spectrum is directly proportional to the number of emitting Eu^{3+} ions and thus to the volume of the nanoparticle [14]. Moreover, they explain why the response of single photoreduced Eu-doped nanoparticles to H_2O_2 and other oxidants varies only slightly from one nanoparticle to another [11,12].

Furthermore, we observe no significant increase in the peak width of single nanoparticle spectra when the doping increases from 10% to 40% [Fig. 4(A)]. Note also that the lattice parameter dependence on doping concentration follows Veggard's law which demonstrates that the Eu^{3+} ions are homogeneously distributed throughout the nanoparticles [3]. The absence of width change implies that the broadening of the peaks is dominated by crystalline imperfections in the nanoparticles and that the effect of doping-related strain, lattice parameter variation or defects is negligible.

Altogether, these results show that Eu-doped vanadate nanoparticles encompass a large number of emission centers homogeneously distributed in a lattice with a microstructure that is similar for all single particles. The measured emission spectrum for single particles reflects the weak but measurable fluctuations of the Eu^{3+}-ion transition energies due to the local crystalline field, averages over the various local structural environments, and is identical for all individual particles.

5. Conclusions

By measuring the emission spectrum of single nanoparticles, we have shown that individual $Y_xEu_{1-x}VO_4$ nanoparticles inside a colloidal nanoparticle solution obtained by a coprecipitation, soft chemistry synthesis route are identical in terms of the distribution of local environments provided for the Eu^{3+} ions. This insight confirms the validity of single-particle level applications of these nanoparticles, in particular in terms of size determination, single-particle tracking, and oxidant sensing. Furthermore, we have developed a sum-frequency blue solid-state laser suitable for direct excitation of Eu^{3+} ions in the visible. The linewidth of the Nd-doped fundamental laser being on the order of a nanometer, it should be possible to tune the sum-frequency emission over a range of 0.5 nm. This could be enough to excite Eu^{3+} ions embedded in other matrices than YVO_4.

Acknowledgments

We acknowledge financial support by the Région Ile-de-France Nanosciences Competence Center through the Eurolase project.